RSC Advances

PAPER

View Article Online
View Journal | View Issue

Cite this: *RSC Adv.*, 2018, **8**, 3151

Crystal growth kinetics, microstructure and electrochemical properties of $LiFePO_4$/carbon nanocomposites fabricated using a chelating structure phosphorus source

Liping He, *[a] Wenke Zha [a] and Dachuan Chen*[b]

$LiFePO_4$/carbon (LFP/C) nanocomposites were fabricated using bis(hexamethylene triamine penta (methylene phosphonic acid)) (BHMTPMPA) as a new and environment-friendly phosphorus source. The activation energy of the fabricated LFP/C was first investigated in depth based on the theoretical Arrhenius equation and experimental results of the LFP/C composite particle size distribution to explore the grain growth dynamics of the LFP/C particles during the sintering process. The results indicate that the activation energy is lower than 3.82 kJ mol^{-1} when the sintering temperature is within the range of 600–800 °C, which suggests that the crystal growth kinetics of the LFP/C particles is diffusion-controlled. The diffusion-controlled mechanism results from the mutual effects of chelation with Fe^{2+} cations, *in situ* formation of carbon layers and high concentration of hard aggregates due to the use of an organic phosphorous source (BHMTPMPA). The diffusion-controlled mechanism of the LFP/C effectively reduces the LFP particle size and hinders the growth of anomalous crystals, which may further result in nanosized LFP particles and good electrochemical performances. SEM and TEM analyses show that the prepared LFP/C has a uniform particle size of about 300 nm, which further confirms the effects of the diffusion-controlled mechanism of the LFP/C particle crystal growth kinetics. Electrochemical tests also verify the significant influence of the diffusion-controlled mechanism. The electrical conductivity and Li-ion diffusion coefficient (D_{Li}^{+}) of the fabricated LFP/C nanocomposite are 1.56×10^{-1} S cm^{-1} and 6.24×10^{-11} cm^2 s^{-1}, respectively, due to the chelating structure of the phosphorus source. The fabricated LFP/C nanocomposite exhibits a high reversible capacity of 166.9 mA h g^{-1} at 0.2C rate, and presents an excellent rate capacity of 134.8 mA h g^{-1} at 10C.

Received 1st November 2017
Accepted 30th December 2017

DOI: 10.1039/c7ra12029j

rsc.li/rsc-advances

Introduction

The development of electric vehicles (EVs) has been greatly promoted due to a greater concern for environmental protection and energy saving worldwide. Lithium-ion batteries (LIBs) play an important role in the next-generation power sources for EVs and intermittent renewable energy.[1,2] As one of the most promising cathode materials in lithium-ion batteries, olivine structured $LiFePO_4$ (LFP) has received considerable attention for LIBs due to its high theoretical specific capacity (170 mA h g^{-1}), intrinsic thermal safety, low cost, and environmental friendliness.[3,4] However, the application of LFP materials has been significantly restricted by the sluggish kinetics of lithium-ion diffusion ($\sim 10^{-14}$ cm^2 s^{-1}) and its intrinsically low electronic conductivity ($\sim 10^{-9}$–10 S^{-10} cm^{-1}).[5] Therefore, to overcome these drawbacks, tremendous efforts have been made to improve the LFP electrode performances by coating electronically conductive agents to increase its surface electronic conductivity,[6–8] doping with foreign cations to enhance its bulk electronic conductivity,[9,10] reducing its particle size and optimizing its particle morphology to facilitate lithium-ion transport.[11–15]

Most of the above considerable research efforts have demonstrated that particle size and microstructure have significant effects on the electrochemical properties of LFP/carbon (LFP/C) composites.[16–18] It is also found that the synthetic conditions for the fabrication of LFP/C, especially the conditions and growth kinetics in the sintering process, are crucial. This can directly determine the crystal growth and particle size, and thus ultimately affect their microstructure and electrochemical performance.[19–21] Generally, the crystal growth kinetics of inorganic materials can be investigated using the Arrhenius equation and the particle size obtained from XRD analysis.[22] The particle size needs to be calculated using the Scherrer and Warren equations based on the XRD results;

[a]*State Key Laboratory of Advanced Design and Manufacturing for Vehicle Body, College of Mechanical & Vehicle Engineering, Hunan University, Changsha, Hunan 410082, P. R. China. E-mail: lphe@hnu.edu.cn; Fax: +86 731 88822051; Tel: +86 731 88823863*
[b]*College of Civil Engineering, Hunan University, Changsha, Hunan 410082, P. R. China. E-mail: 13707311929@163.com*

however, application of the calculation is inherently limited to crystalline materials.[23] In fact, the particle size can also be obtained directly using the experimental results from the particle size distribution, which is more widely available and practical to investigate the particle growth kinetics in the crystals or amorphous materials. Nevertheless, thus far, the crystal growth kinetics of LFP materials during the sintering process has rarely been investigated using the Arrhenius equation as the fundamental theory,[24] and especially no work has been reported on the investigation into the crystal growth kinetics of LFP/C materials based on the particle size obtained directly from experimental data from the particle size distribution. Therefore, the present work tries to investigate the crystal growth kinetics of LFP/C materials based on the theoretical Arrhenius equation and experimental results of the LFP/C composite particle size distribution and reveal the relationship among the crystal growth thermodynamics, microstructure and electrochemical properties of the fabricated LFP.

H_3PO_4 or $NH_4H_2PO_4$ is normally used as the phosphorus source in the synthesis of LFP.[25,26] However, the synthetic process is not environmentally friendly and it easily leads equipment corrosion. Moreover, extra carbon sources or surfactants also need to be added to obtain the C-coating or nanosized LFP particles.[27,28] Recently, the organic phosphorous acid, bis(hexamethylene triamine penta (methylenephosphonic acid)) (BHMTPMPA), which is abundant, low-cost, and eco-friendly, was used to synthesize a wide range of inorganic materials with novel microstructures and properties.[29,30] BHMTPMPA, with the chemical formula $C_{17}H_{44}O_{15}N_3P_5$, has a high phosphorus and carbon content and especially has some chelation functional groups in its molecule, as shown in Fig. 1. Therefore, the present work attempts to use BHMTPMPA ($C_{17}H_{44}O_{15}N_3P_5$) as a new phosphorus source instead of the commonly used H_3PO_4 or $NH_4H_2PO_4$. It is expected that this new organic phosphorus source will have a pronounced influence on the crystal growth and size of the LFP particles, and thus on the microstructure and electrochemical properties of the fabricated LFP/C composites due to the special characteristics of BHMTPMPA, such as its inherent symmetrically distributed organic linking units, high phosphorus content and chelating function groups.

Overall, the present work develops a new method for the fabrication of LFP/C nanocomposites using BHMTPMPA as a new phosphorus source. The crystal growth thermodynamics and activation energy of the fabricated LFP/C are investigated using the experimental results of particles size distribution and the fundamental theory of the Arrhenius equation in order to explore the grain growth kinetics of the fabricated LFP/C particles during the sintering process. Meanwhile, this work also investigates in depth the effects of the organic phosphorus source (BHMTPMPA) on the microstructure and electrochemical properties of the fabricated LFP/C nanocomposites.

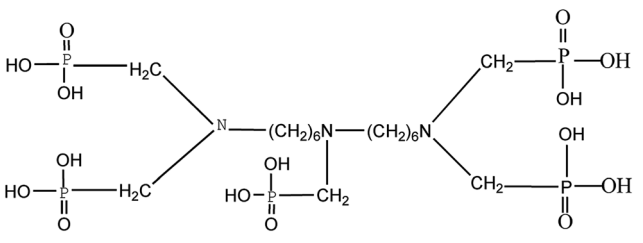

Fig. 1 Molecular structure of the organic phosphorous source BHMTPMPA.

Fundamental theories

The Arrhenius equation is a formula that describes the temperature dependence of reaction mechanisms.[31,32]

$$D_t = D_0 e^{-RT/Q} \quad (1)$$

where, D_0 and D_t denote the initial and final composite sizes (nm), R is the gas constant (8.314 kJ mol^{-1}), and T is the sintering temperature (K). This equation has vast and crucial application in determining the kinetics of chemical reactions and calculation of their activation energy. Generally, the crystal growth kinetics of inorganic crystal materials during the sintering process includes two types of mechanisms: the diffusion-controlled mechanism and interface reaction controlled mechanism.[33–36] Normally the activation energy is less than 300 kJ mol^{-1} if the crystal growth thermodynamics during the sintering reaction process is determined by the diffusion-controlled mechanism. The diffusion controlled mechanism can effectively inhibit the grain growth of crystals particles and yield a positive effect on controlling the particle size of fabricated materials; whereas the interface reaction controlled mechanism is usually associated with a higher activation energy (higher than 300 kJ mol^{-1}), and usually leads to the growth of anomalous crystals.[34,35] In the present work, the activation energy of the fabricated LFP/C nanocomposites was calculated based on the Arrhenius equation in combination with experimental particle size distribution data to elucidate the grain growth kinetics of the LFP/C particles during the sintering process.

Experimental

Preparation of LFP/C nanocomposites

LFP/C nanocomposites were fabricated using BHMTPMPA ($C_{17}H_{44}O_{15}N_3P_5$) as the phosphorus source *via* a hydrothermal method in an autoclaved stainless-steel reaction vessel. All chemicals used were analytical grade commercial products. In a typical fabrication procedure, a stoichiometric solution of LiOH, $FeSO_4$ and BHMTPMPA was mixed in a ratio of 15 : 5 : 1 to obtain a molar ratio of Li/Fe/P = 3 : 1 : 1 in the LFP material. First, $FeSO_4 \cdot 7H_2O$ and BHMTPMPA were dissolved in deionized water successively under constant stirring for 30 min to obtain a homogeneous and transparent solution. $LiOH \cdot H_2O$ solution was then slowly added to the above mixture under magnetic stirring for 30 min and bubbling with high-pure Ar. Subsequently, the prepared precursor was quickly transferred to a stainless-steel autoclave and heated at 180 °C for 6 h. The autoclave was subsequently cooled to room temperature and

the resulting green precipitate was collected from the autoclave and washed, filtered, and dried at 60 °C for 12 h. Finally, the powder was sintered in a tube furnace at 600 °C, 650 °C, 700 °C, 750 °C and 800 °C for 60 min, 90 min, 120 min, 150 min, and 180 min, respectively, at a heating rate of 10 °C min^{-1} and under a high-purity Ar atmosphere to obtain the LFP/C nanocomposites.

Material characterization

The crystal structures of the LFP/C nanocomposites were characterized *via* X-ray diffraction (XRD) (Bruker AXS, D8 Advance) on an instrument equipped with a Cu Kα radiation source and operated at 45 kV and 200 mA. The microstructure and elemental analysis of LFP/C were characterized *via* scanning electron microscopy (SEM, Hitachi, S-4800) and transmission electron microscopy (TEM, JEOLJEM-2100F) on an instrument equipped with an energy-dispersive X-ray microanalysis system (EDX), respectively. The particle size distribution of the prepared LFP/C nanocomposites fabricated at different sintering temperatures and times were analyzed on a Zetasizer Nano ZS (Malvern Instruments, Malvern, UK) with a 633 nm helium–neon laser using back-scattering detection. The average particle size and polydispersity index (PDI) of LFP/C were analyzed using the associated Zetasizer software (Dispersion Technology Software v 5.00, Malvern).

Electrochemical measurements

Electrochemical properties were measured using CR2032 coin-type cells, which were assembled in a glove box filled with high purity argon. A mixture of LFP/C nanocomposites, acetylene black, and poly(vinyl difluoride) (PVDF) at a weight ratio of 80 : 10 : 10 was coated uniformly onto Al foil. The electrodes were dried at 65 °C for 6 h, then roll-pressed and further dried at 65 °C for 12 h in a vacuum oven. Pure lithium foil was utilized as the negative electrode while a micro-porous membrane (Celgard 2400) was employed as the separator. 1 M $LiPF_6$ dissolved in a mixture of ethylene carbonate (EC)/dimethyl carbonate (DMC) (1 : 1, v/v) was used as the electrolyte. Galvanostatic charge/discharge, rate and cycle performance measurements for the assembled cells were conducted using a Neware Battery Test System (BTS-9000, Shenzhen Neware Electronic Co. Ltd., P. R. China) in the potential range of 2.5–4.2 V (Li^+/Li) at room temperature (25 °C). Electrochemical impedance spectra (EIS) measurements were performed in the frequency range of 100 kHz to 10 MHz on a CHI660B electrochemical workstation (Chenhua, Shanghai, China) with an AC amplitude of 5 mV. The electrical conductivity of the cathode films was tested using the four-point DC method with an S-2A probe station equipped with an Agilent 34401A ammeter and a Keithley 2400 voltmeter.

Results and discussion

Crystal growth kinetics of the LFP/C nanocomposites

Fig. 2a shows the particle size distribution of the LFP/C composites obtained at 700 °C for 150 min, which was measured using a Malvern laser particle size analyzer. The results show that LFP/C is a nano-sized composite with a narrow particle size distribution (ranging from 112 to 551 nm). Additionally, the polydispersity index (PDI) is a parameter that reflects particle size monodispersity.[37] It can be clearly seen from Fig. 2a that the PDI is 0.074 and the average particle diameter is 303.1 nm with a maximum diameter of 330.2 nm, which demonstrate that the LFP/C particles have good monodispersity and uniform particle size, respectively. The LFP/C nanocomposites prepared at different temperatures and times have similar particle size trends and small PDI. The obtained average particle size of LFP/C was applied to the Arrhenius equation to calculate the activation energy and investigate the crystal growth kinetics of the LFP/C nanocomposites. Fig. 2b shows the average particle size at different temperatures and times. It is obvious that the average particle size of the LFP/C composites increases with an increase in the sintering temperature. The average particle size of LFP/C varies from 135 nm to 470 nm as the sintering time increases from 60 min to 180 min with the sintering temperature in the range of 600–800 °C. Furthermore, it is also found that when the sintering time is fixed within 90–120 min, the average particles sizes of LFP/C sintered at 600 °C, 650 °C, 700 °C, 750 °C and 800 °C increased by 15 nm, 52 nm, 105 nm, 90 nm, and 113 nm, respectively. The increase rate of the average particle size of LFP/C mainly presents an increasing trend with an increase in the sintering temperature. This is because the higher the sintering temperature, the greater the driving force for crystal growth, and consequently, larger particle sizes. Additionally, the increase rate in the average particle size of LFP/C increases first between 600–700 °C, subsequently decreases at 750 °C and then increases at 800 °C. An inflection point occurs at a sintering temperature of 750 °C, which indicates that the sintering temperature of 700–750 °C is suitable form fine crystal LFP/C composites, which is further verified by the calculation results of the activation energy and experimental results of the electrochemical measurements. Furthermore, in the time range of 150–180 min, the increase in the LFP/C average particle size becomes slower, which suggests that the sintering time of 150 min is the rapidest period of crystal nucleation and growth in the LFP/C nanocomposites. Especially, the fabricated LFP/C composite (700 °C, 150 min) has an ordered olivine crystal structure with a unit cell volume of 292.959 $Å^3$ and nano-spherical structure with a diameter of about 300 nm, which are further confirmed by the XRD and TEM results (Fig. 5 and 7a and b), respectively. When the sintering temperature is higher than 700 °C, the average particle sizes of the LFP/C composites are 375 nm and 445 nm at 750 °C and 800 °C, respectively. This could be because that the grain boundary may migrate faster under a higher temperature, resulting in secondary growth of the LFP/C, which leads to a larger LFP/C composite particle size.

Fig. 2c shows the activation energy curves of the LFP/C nanocomposites at different annealing times. It is assumed that the crystal growth of the LFP/C nanocomposites is a thermally activated process, which is dependent on the sintering temperature according to the Arrhenius equation.[35,36] Thus, Fig. 2b is replotted as Fig. 2c by taking the logarithm and linear fitting based on the Arrhenius equation. Hence, the activation

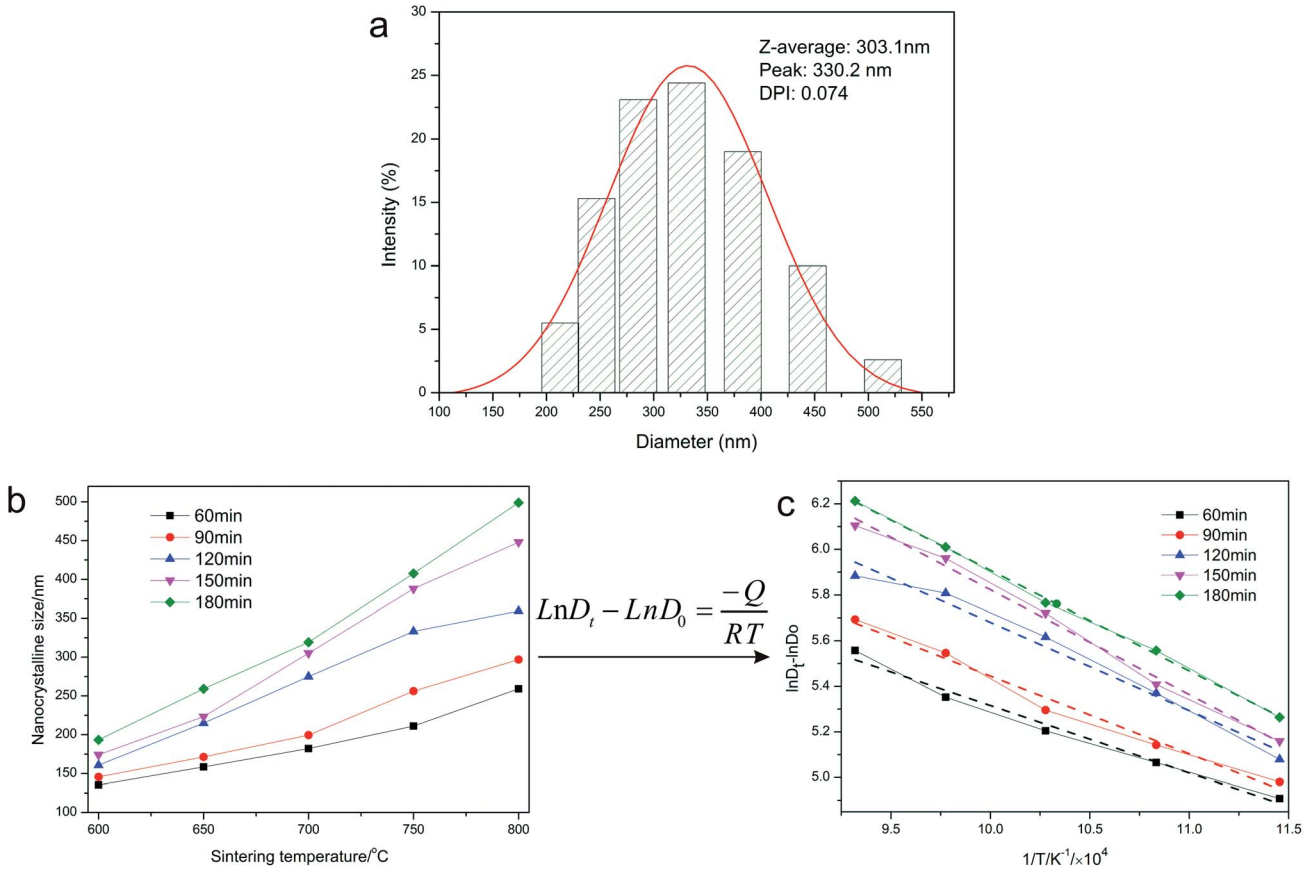

Fig. 2 (a) Size distribution of the LFP/C nanocomposite (700 °C, 150 min), (b) effects of sintering temperature and time on the average particle size of the LFP/C nanocomposite and (c) activation energy curves for the LFP/C nanocomposites at different sintering times.

energy (Q, kJ mol^{-1}) of LFP/C can be calculated from the slope ($-Q/R$) of the curves in Fig. 2c, and the calculation results are shown in Fig. 3.

The activation energy for the crystal growth of the LFP/C nanocomposites increases stepwise when the sintering time is in the range of 60–150 min, reaches the maximum at 150 min and then decreases rapidly. This result is identified from the increasing trend of the LFP/C particle size (Fig. 2b) and confirms that the optimized fabrication condition of the LFP/C nanocomposite is the sintering time of 150 min. In addition, it is also found that the highest activation energy of LFP/C crystal growth is ~3.82 kJ mol^{-1} at 150 min, which suggests that the crystal growth kinetics of the LFP/C composite with BHMTPMPA as the phosphate source is determined by the diffusion-controlled mechanism based on the fundamental theories of crystal growth in inorganic materials.[33–36] The diffusion controlled mechanism of the LFP/C crystal growth kinetics can effectively inhibit the secondary growth of LFP, thus yielding a positive effect on controlling the particle size of the fabricated LFP/C nanocomposite, which could be confirmed by the microstructure results (Fig. 7a and b).

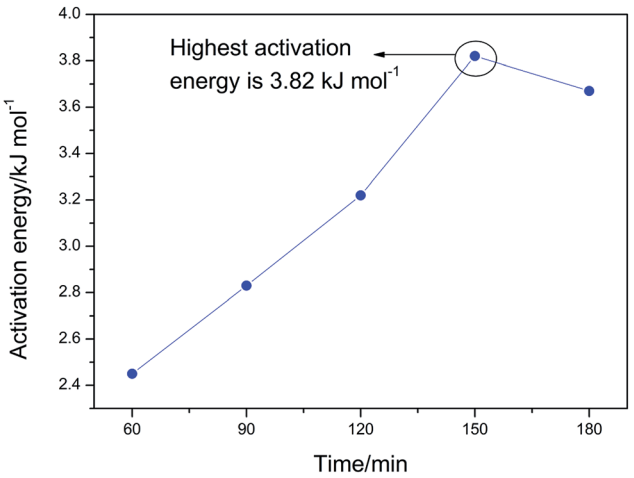

Fig. 3 Activation energy of the LFP/C nanocomposites at different sintering times.

In the present work, the mechanism for the diffusion controlled crystal growth kinetics of the LFP/C nanocomposite is further investigated and schematically illustrated in Fig. 4. First, BHMTPMPA coordinates with Fe^{2+} ions through its hexa-coordinate chelating functional groups, and *in situ* forms carbon layers around the LFP particles which especially reduce the activation energy of the grain formation between the LFP/C particles. Second, hard aggregates (indicated by the dotted circles in Fig. 4) mat be formed based on the very low activation

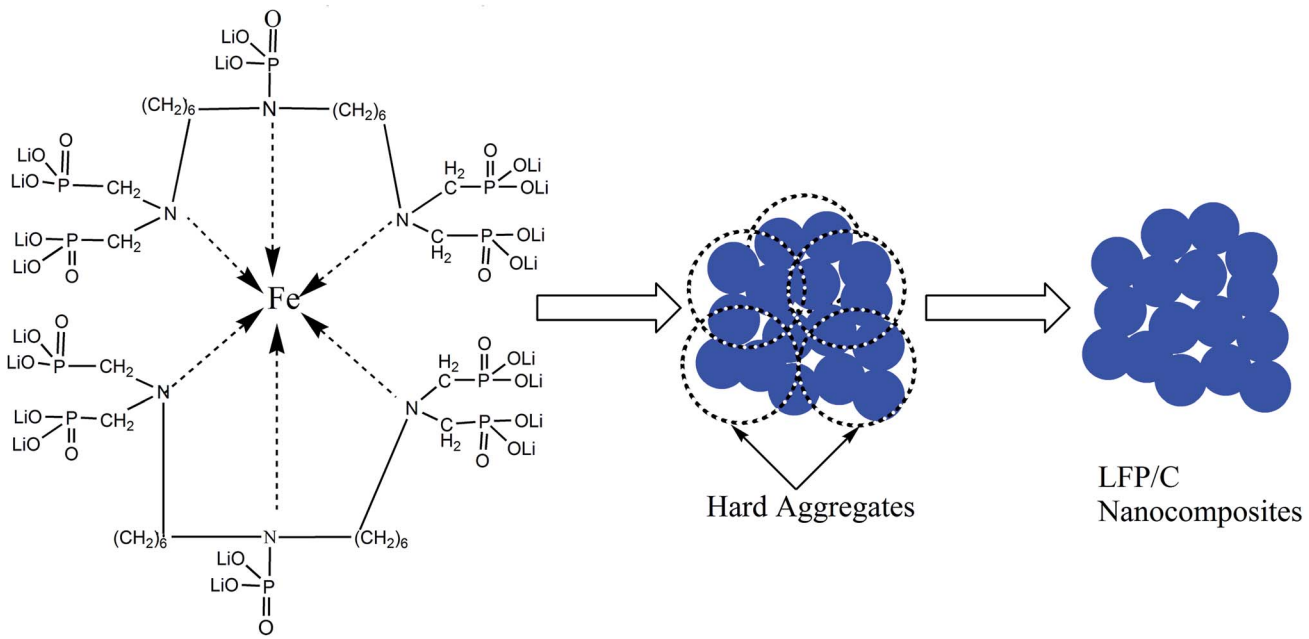

Fig. 4 Schematic presentation of the diffusion controlled crystal growth kinetics of the LFP/C nanocomposite.

energy or even a zero-kinetic barrier in a rotation process, which change the grain orientation and decrease the angle of misorientation. During the sintering treatment of LFP/C, the increase in particle size is mainly dependent on the elimination of boundaries between the LFP nanocrystals within the hard aggregates. As a result, the average size of the uniform LFP nanoparticles may be inclined to approach the average size of the hard aggregates, resulting in a single LFP nano-crystal, which is further well confirmed by the XRD results. Hence, it appears that the combined effect of chelation with Fe^{2+} cations, *in situ* formation of carbon layers and high concentration of hard aggregates resulting from the new phosphate source (BHMTPMPA) drastically reduce the grain growth activation energy, thus enhancing the rate and efficiency of diffusion control.

Microstructure of LFP/C nanocomposite

Fig. 5 shows the XRD patterns of the LFP/C nanocomposite at 700 °C for 150 min. It is obvious that the diffraction patterns perfectly exhibit single phase $LiFePO_4$ with an ordered olivine structure, which is indexed to the orthorhombic *Pnma* space group (JCPDS no. 40-1499).[38] Clearly, all the diffraction peaks are narrow and strong, which indicate the high purity of the synthesized LFP/C nanocomposite. The lattice parameters of the LFP/C composite were analyzed using the Rietveld refinement method in the Jade 5.0 software. The calculated lattice parameters of the fabricated LFP/C composite are $a = 6.0297$ Å, $b = 10.298$ Å, and $c = 4.7123$ Å, with a final unit volume of 292.605 Å^3. These lattice parameters are very close to that of pristine $LiFePO_4$ (JCPDS no. 40-1499) ($a = 6.019$ Å, $b = 10.347$ Å, $c = 4.704$ Å, and $V = 292.959$ Å^3).[6,38] Furthermore, there is no obvious carbon diffraction peak in the XRD pattern of the LFP/C nanocomposite, which is most probably due to the low content of carbon or carbon in the amorphous form.[39] In addition, the LFP/C composites prepared at different temperatures and times present similar XRD diffraction results to the nanocomposite obtained at 700 °C for 150 min.

Raman spectroscopy is an important technique to investigate the properties of carbon phases that cannot be detected by XRD, and the result of the LFP/C composite (at 700 °C for 150 min) is shown in Fig. 6. Two broad bands are detected at around 1345 and 1573 cm^{-1} in the spectrum, which are ascribed to the D band (disorder band) and G band (graphitic band), respectively. The peak intensity ratio of the D band to G band (I_D/I_G) is inversely proportional to the graphitization degree of carbon. Normally the higher the degree of graphitization, the higher the

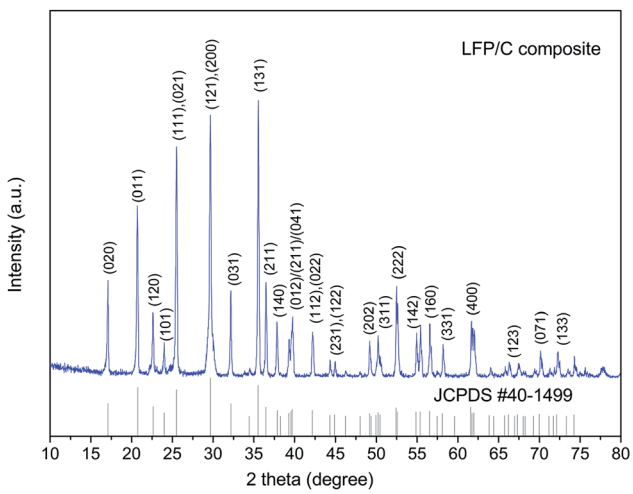

Fig. 5 XRD of LFP/C at 700 °C for 150 min.

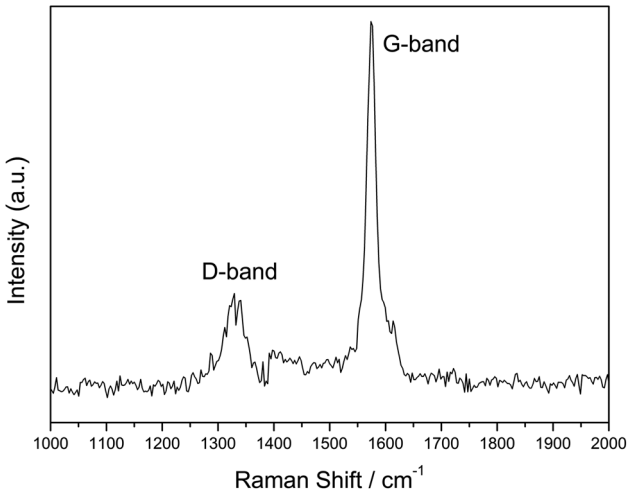

Fig. 6 Raman spectrum of LFP/C obtained at 700 °C for 150 min.

electronic conductivity of carbon, and the better the electrochemical performances achieved. Therefore, if the value of I_D/I_G is very low, it suggests that the amount of graphitic carbon (sp^{2-} coordinated carbon) is much more than disordered carbon (sp^{3-} coordinated carbon).[5,27] The calculated value of I_D/I_G of the fabricated LFP/C composite is about 0.47, which indicates that the carbon in the LFP/C composite mainly exists as a graphite-like structure due to the *in situ* carbon formed from the chelating structure phosphorus source.

Fig. 7 shows the SEM and high TEM images of the LFP/C nanocomposite sintered at 700 °C for 150 min. The LFP/C particles are uniform with a nanospherical structure and a diameter of about 300 nm. The EDX analysis indicates that the atomic ratio among P, Fe, O, and C is about 6 : 9 : 37 : 4 as shown in Fig. 7d (EDX results do not show lithium element due to its low electron-scattering cross section),[40,41] which indicates that the new phosphorus source successfully *in situ* formed nanosized carbon layers. Obviously, the *in situ* carbon is well-distributed around each LFP particle with an average layer thickness of 2–5 nm (Fig. 7c). Similarly, the LFP/C nanocomposites prepared at other temperatures and times have analogous solid nanospherical structures with different particles sizes. These results indicate that the use of BHMTPMPA as a phosphorus source successfully produces LFP with high crystallinity and narrow and uniform nanoscale particle size distributions, which are important factors for excellent electrochemical performances in LIB electrode materials. Furthermore, the *in situ* grown carbon layers covered on the LFP particles may form an effective conducting network to enhance the surface electronic conductivity of the nanocomposites, and hence promotes the electrochemical reaction during charge/discharge processes.[42,43] This is confirmed by the electrochemical tests of the LFP/C nanocomposites, as shown below.

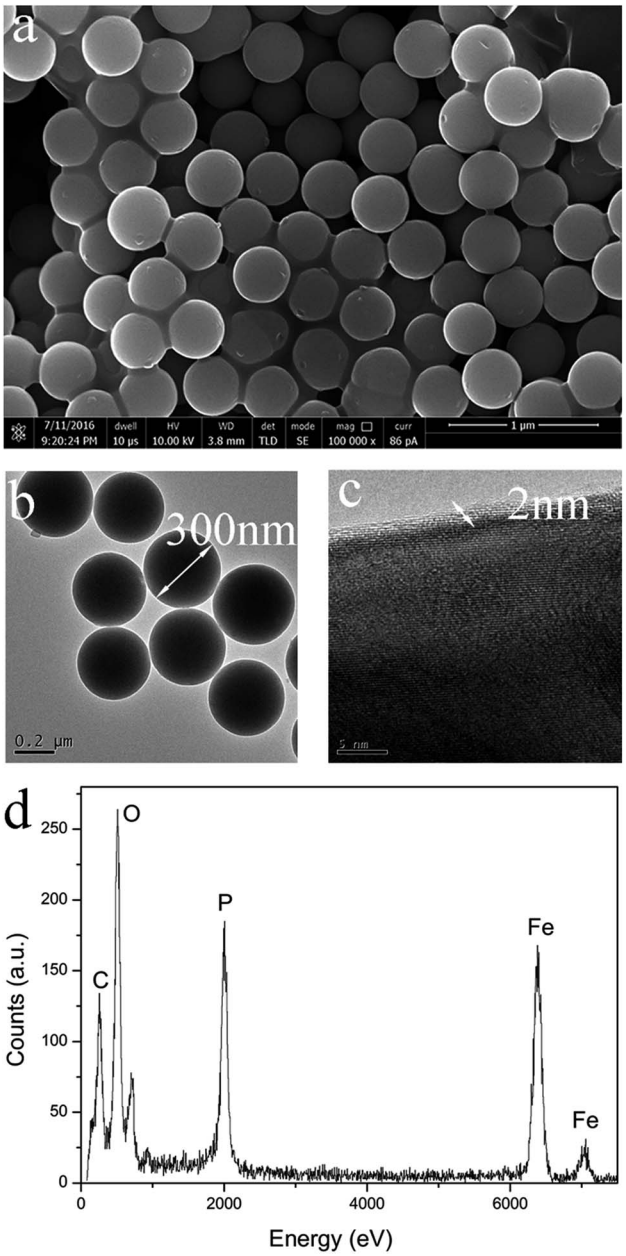

Fig. 7 Microstructure of LFP/C obtained at 700 °C for 150 min. (a) SEM image, (b and c) HR-TEM images, and (d) EDX analysis.

Electrochemical properties of LFP/C nanocomposites

Fig. 8a shows the discharge capacity of the LFP/C nanocomposites fabricated at different temperatures and sintering times at 0.2C. Clearly, the discharge capacity of LFP/C firstly increases, then decreases at 600 °C, 650 °C, 700 °C, and reaches the maximum at 150 min. In contrast, although the discharge capacity of LFP/C presents a similar variation trend, the highest discharge capacity is reached at 120 min for 750 °C and 800 °C. Furthermore, the highest discharge capacity of LFP/C is recorded at 700 °C for 150 min which is consistent with the results of the particle size distribution and activation energy calculation. Hence, the LFP/C nanocomposite prepared at 700 °C for 150 min was selected to investigate the effect of BHMTPMPA on the charge/discharge capacity, rate and cycle performances.

Fig. 8b depicts the typical initial charge/discharge curves of the LFP/C nanocomposite (700 °C, 150 min) over the voltage

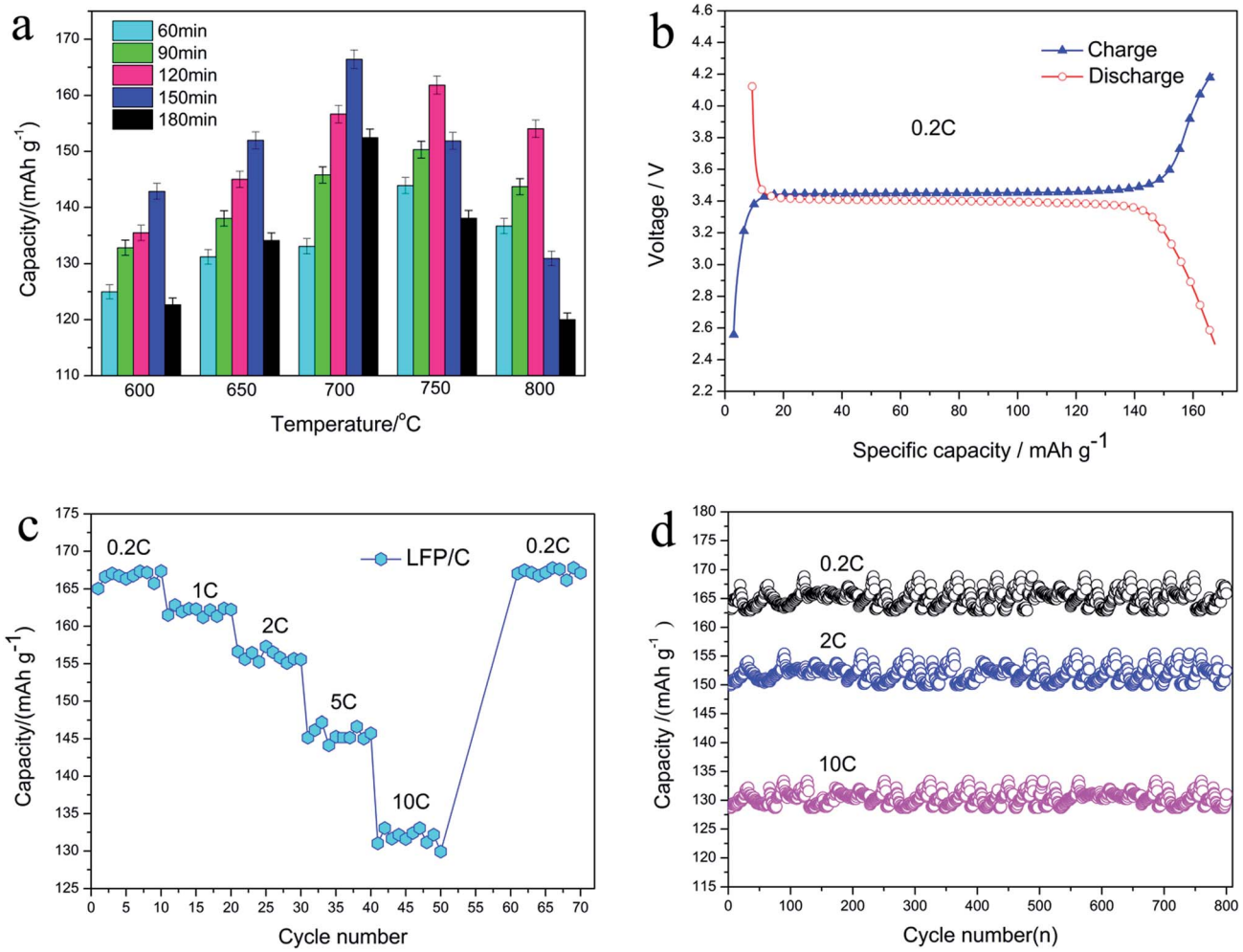

Fig. 8 (a) Discharge capacity of the LFP/C nanocomposites obtained at different sintering temperatures and times at 0.2C. LFP/C nanocomposite (700 °C, 150 min) (b) initial charge/discharge curves between 2.5 and 4.2 V at 0.2C, (c) rate performances and (d) cycle performance at different discharge currents.

range of 2.5–4.2 V at a current density of 0.2C. It is found that the electrodes display a flat discharge plateau at around 3.4 V which is slightly higher than that of previously reported LFP composites.[17,39,42] At a current density of 0.2C, the LFP/C nanocomposite electrode exhibits a specific discharge capacity of 166.9 mA h g^{-1}. This suggests that the specific capacity of the prepared LFP/C nanocomposite can be notably improved due to the nano-effect and effect of the *in situ* grown carbon, which are due to the chelating organic functional groups (especially the symmetrical hexa-coordinate N atoms) in the BHMTPMPA molecule and diffusion-controlled crystal growth kinetics in the sintering process.

Fig. 8c compares the rate performances of the LFP/C nanocomposite (700 °C, 150 min) at different discharge rates. The C-rate increases stepwise from 0.2C to 10C. At a low current rate of 0.2C, LFP/C delivers 168–165 mA h g^{-1} while its capacity decreases gradually as the rate increases. In particular, it can maintain enhanced capacities even at high C-rates, for instance at 10C, the LFP/C nanocomposite presents the average discharge capacity of 134.8 mA h g^{-1} (corresponding to 79.3% of the theoretical capacity). The rate performance of LFP/C at different discharge rates is better than that reported in the literature.[21,43] After cycling at various rates when the current returns to 0.2C, the original discharge capacity can be recovered. This demonstrates that the nanospherical structure of LFP/C has good stability and high tolerance to various charge/discharge currents, which is a crucial desirable property for lithium-ion battery materials.

Fig. 8d presents the cycle performances of the LFP/C nanocomposite (700 °C, 150 min) electrode at various charge/discharge current rates. It can be seen that the LFP/C nanocomposite retains discharge capacities of 165.6 and 151.7 mA h g^{-1} at a rate of 0.2 and 2C after 800 charge/discharge cycles, which correspond to a capacity retention of 93.8% and 87.3%, respectively. This is superior than the values for LFP/C reported in the literature at the same testing conditions.[8,44,45] Additionally, LFP/C also shows an 800th cycle discharge capacity of 130.2 mA h g^{-1} at a high rate of 10C, which confirms its stable cycling capability with 76.6% retention. The improved rate capability and excellent cycling stability can be attributed to

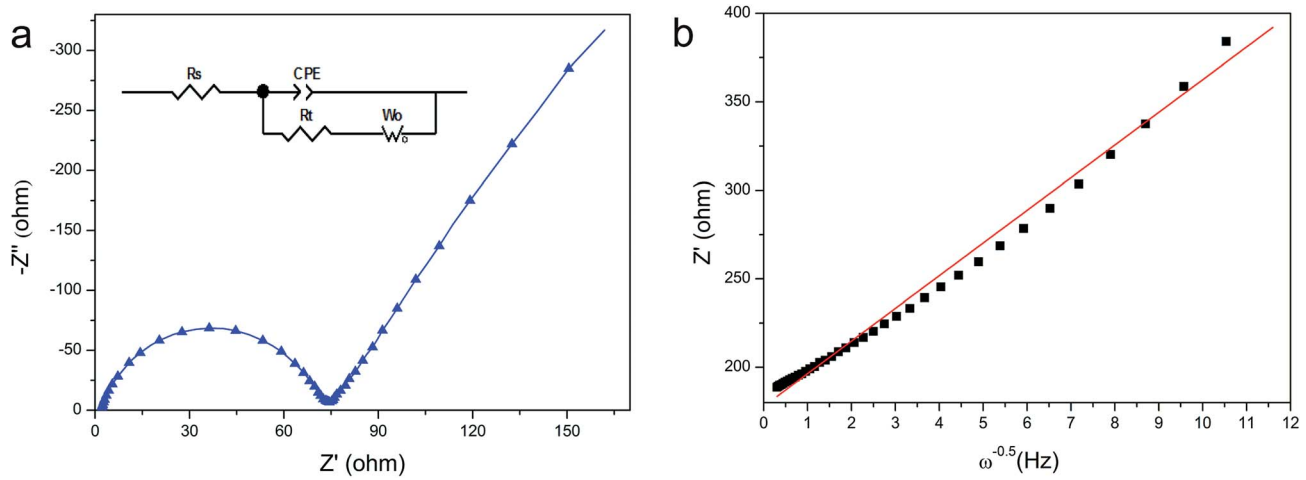

Fig. 9 (a) Impedance spectra of the LFP/C composite (700 °C, 150 min). (b) Relationship between Z' and $\omega^{-0.5}$ in the low-frequency region.

the solid nanospherical structure of LFP/C built from the chelation and activation energy reduction effects of BHMTPMPA, which enhance the electronic conductivity and hinder stress from the volume expansion/shrinkage of the LFP particles during the charge/discharge processes.[7,39,41]

The electrochemical performance of the fabricated LFP/C composite (700 °C, 150 min) was also investigated *via* electrochemical impedance spectroscopy (EIS). The Nyquist graph of the LFP/C composite (700 °C, 150 min) is presented in Fig. 9a, and an equivalent circuit was established to simulate and analyze the impedance spectra. The intercept at the Z-axis in the high frequency region is associated with R_s, which includes electrolyte solution resistance and electric contact resistance. The semicircle in the high and middle frequency range represents the charge transfer resistance (R_{ct}) at the electrode and the straight line in the lower frequency is attributed to the lithium-ion diffusion resistance in the electrode, namely the Warburg impedance.[12,43] It is clear that the LFP/C composite shows a lower R_{ct} value (~75 Ω) than that of pristine $LiFePO_4$ (~120 Ω).[4,10] The impedance is inversely proportional to electrical conductivity, which suggests a high charge transfer rate for the fabricated LFP/C composite. This is in good agreement with the rate and cycle performances of the fabricated LFP/C composite. Actually, the electrical conductivity of the LFP/C composite (700 °C, 150 min) according to the four-point DC method reaches 1.56×10^{-1} S cm^{-1}, which is nearly nine orders of magnitude higher than that of pristine $LiFePO_4$ (10^{-9}–10^{-10} S cm^{-1}).[11,28,42] This clearly indicates that the electrical conductivity of the LFP/C composite is remarkably enhanced by the *in situ* grown carbon covering on the spherical LFP nanoparticles, which resulted from the effects of the inherent symmetrically distributed organic linking units and chelating function groups in BHMTPMPA.

Furthermore, the Li-ion diffusion coefficient (D_{Li}^+, cm^2 s^{-1}) is also an important factor related to the electrochemical performances of lithium-ion battery cathode materials. The D_{Li}^+ of the fabricated LFP/C composite (700 °C, 150 min) was calculated using eqn (2):[8,17]

$$D_{Li^+} = \frac{R^2T^2}{2A^2n^4F^4C^2\sigma^2} \quad (2)$$

where, R is the gas constant (8.314 kJ mol^{-1}), T is the absolute temperature (298.15 K), A is the surface area of the cathode (cm^2), n is the number of electrons per molecule during oxidation (1 in this case), F is the Faraday constant (96 500C mol^{-1}), C is molar concentration of Li ions, and σ is the Warburg impedance coefficient. σ for the LFP/C composite (700 °C, 150 min) is about 18.46 cm^2 $s^{-0.5}$, which was obtained from the slope of the plot of Z_{Re} and square root of frequency ($\omega^{-0.5}$) in the low frequency region (as shown in Fig. 9b) based on eqn (3).[41]

$$Z_{Re} = R_e + R_{ct} + \sigma\omega^{-0.5} \quad (3)$$

The D_{Li}^+ of the LFP/C composite calculated based on the obtained Warburg impedance coefficients (σ) is about 6.24×10^{-11} cm^2 s^{-1}, which is almost ~3 orders of magnitude higher than that of pristine $LiFePO_4$ (~10^{-14} cm^2 s^{-1}).[6,25] The improvement in the Li-ion diffusion coefficient can be attributed to the uniform nanospherical structure of the fabricated LFP/C composite and *in situ* formed carbon resulting from the chelation and activation energy reduction effects of BHMTPMPA.

Conclusions

(1) In the present work, LFP/C nanocomposites with carbon *in situ* formed on LFP were fabricated using bis(hexamethylene triamine penta (methylenephosphonic acid)) (BHMTPMPA) as a new and environmentally friendly phosphorus source.

(2) The activation energy of the fabricated LFP/C is lower than 3.82 kJ mol^{-1} and its crystal growth kinetics is diffusion-controlled.

(3) The diffusion-controlled mechanism is attributed to the integrated effects resulting from the use of an organic phosphorous source (BHMTPMPA), *i.e.*, chelation with Fe^{2+} cations, which induces the *in situ* formation of carbon layers and the

hard aggregation effect of the LFP/C particles, thus reducing the LFP particle size and optimizing the particle morphology.

(4) The prepared LFP/C nanocomposite (700 °C, 150 min) exhibits a uniform solid nanospherical structure with a diameter of ~300 nm and discharge capacity of 130.2 mA h g^{-1} even at a high rate of 10C with a capacity retention of 76.6% after 800 cycles due to the diffusion-controlled crystal growth of the LFP/C particles.

(5) The LFP/C nanocomposite (700 °C, 150 min) fabricated using an organic phosphorous source presents enhanced electrical conductivity and Li-ion diffusion coefficient compared to LFP/C synthesized using a conventional phosphorous source. This will be beneficial to further improve the electrochemical performances of LFP/C composites.

Conflicts of interest

There are no conflicts to declare.

Acknowledgements

This work was supported by the "863" Hi-tech project from the Ministry of Science and Technology of China (grant number 2008AA030905), the Natural Science Foundation of China (grant number 51073051), the Fund from the State Key Laboratory of Advanced Design and Manufacturing for Vehicle Body (grant number 71475003), and 111 Project (grant number B16015).

Notes and references

1 M. S. Whittingham, *Chem. Rev.*, 2014, **114**, 11414–11443.
2 W. Waag, C. Fleischer and D. U. Sauer, *J. Power Sources*, 2014, **258**, 321–339.
3 A. Eftekhari, *J. Power Sources*, 2017, **343**, 395–411.
4 A. K. Padhi, K. Nanjundaswamy and J. B. Goodenough, *J. Electrochem. Soc.*, 1997, **144**, 1188–1194.
5 Q. Zhao, Y. Zhang, Y. Meng, Y. Wang, J. Ou, Y. Guo and D. Xiao, *Nano Energy*, 2017, **34**, 408–420.
6 J. Pang, R. G. Mendes, P. S. Wrobel, M. D. Wlodarski, H. Q. Ta, L. Zhao, L. Giebeler, B. Trzebicka, T. Gemming and L. Fu, *ACS Nano*, 2017, **11**, 1946–1956.
7 K. Zhang, J.-T. Lee, P. Li, B. Kang, J. H. Kim, G.-R. Yi and J. H. Park, *Nano Lett.*, 2015, **15**, 6756–6763.
8 X. Guo, Q. Fan, L. Yu, J. Liang, W. Ji, L. Peng, X. Guo, W. Ding and Y. Chen, *J. Mater. Chem. A*, 2013, **1**, 11534–11538.
9 A. Paolella, G. Bertoni, P. Hovington, Z. Feng, R. Flacau, M. Prato, M. Colombo, S. Marras, L. Manna and S. Turner, *Nano Energy*, 2015, **16**, 256–267.
10 R. He, Z. Liu, L. Zhang, R. Guo and S. Yang, *J. Alloys Compd.*, 2016, **662**, 461–466.
11 J. Wang and X. Sun, *Energy Environ. Sci.*, 2015, **8**, 1110–1138.
12 Y. Liu, J. Gu, J. Zhang, J. Wang, N. Nie, Y. Fu, W. Li and F. Yu, *Electrochim. Acta*, 2015, **173**, 448–457.
13 Y. Zhang, H. J. Zhang, Y. Y. Feng, L. Fang and Y. Wang, *Small*, 2016, **12**, 516–523.
14 L. Bao, G. Xu, X. Sun, H. Zeng, R. Zhao, X. Yang, G. Shen, G. Han and S. Zhou, *J. Alloys Compd.*, 2017, **708**, 685–693.
15 X. L. Wu, Y. G. Guo, J. Su, J. W. Xiong, Y. L. Zhang and L. J. Wan, *Adv. Energy Mater.*, 2013, **3**, 1155–1160.
16 J. Liu, M. N. Banis, Q. Sun, A. Lushington, R. Li, T. K. Sham and X. Sun, *Adv. Mater.*, 2014, **26**, 6472–6477.
17 W.-J. Zhang, *J. Power Sources*, 2011, **196**, 2962–2970.
18 L.-H. Hu, F.-Y. Wu, C.-T. Lin, A. N. Khlobystov and L.-J. Li, *Nat. Commun.*, 2013, **4**, 1687.
19 Y. Huang, H. Liu, Y.-C. Lu, Y. Hou and Q. Li, *J. Power Sources*, 2015, **284**, 236–244.
20 L. He, W. Zha and D. Chen, Effects of organic phosphorus acid on the core-shell structure and electrochemical properties of $LiFePO_4$ uniformly wrapped with in-situ growed graphene nanosheets, *J. Alloys Compd.*, 2017, **727**, 948–955.
21 M. Chen, K. Kou, M. Tu, J. Hu, X. Du and B. Yang, *Solid State Ionics*, 2017, **310**, 95–99.
22 A. Richter, J. Benick, M. Hermle and S. W. Glunz, *Appl. Phys. Lett.*, 2014, **104**, 061606.
23 G. Patermarakis and N. Papandreadis, *Electrochim. Acta*, 1993, **38**, 2351–2361.
24 X. Yang, D. Liu, X. Xu, X. He and J. Xie, *CrystEngComm*, 2013, **15**, 10648–10656.
25 L. Dimesso, C. Förster, W. Jaegermann, J. Khanderi, H. Tempel, A. Popp, J. Engstler, J. Schneider, A. Sarapulova and D. Mikhailova, *Chem. Soc. Rev.*, 2012, **41**, 5068–5080.
26 T. Sui, B. Song, J. Dluhos, L. Lu and A. M. Korsunsky, *Nano Energy*, 2015, **17**, 254–260.
27 J.-c. Zheng, Y.-d. Han, B. Zhang, C. Shen, L. Ming and J.-f. Zhang, *ACS Appl. Mater. Interfaces*, 2014, **6**, 13520–13526.
28 J. M. Patete, M. E. Scofield, V. Volkov, C. Koenigsmann, Y. Zhang, A. C. Marschilok, X. Wang, J. Bai, J. Han and L. Wang, *Nano Res.*, 2015, **8**, 2573–2594.
29 Y.-P. Zhu, T.-Z. Ren and Z.-Y. Yuan, *Catal. Sci. Technol.*, 2015, **5**, 4258–4279.
30 N. Stock and T. Bein, *Angew. Chem., Int. Ed.*, 2004, **43**, 749–752.
31 K. B. Andersen and V. Esposito, *J. Eur. Ceram. Soc.*, 2014, **34**, 3769–3778.
32 T. K. Roy, D. Bhowmick, D. Sanyal and A. Chakrabarti, *Ceram. Int.*, 2008, **34**, 81–87.
33 S.-G. Chen, Y.-S. Yin, D.-P. Wang and J. Li, *J. Cryst. Growth*, 2004, **267**, 100–109.
34 M. Maley, J. Willis, H. Lessure and M. McHenry, *Phys. Rev. B*, 1990, **42**, 2639.
35 S. Shukla, S. Seal, R. Vij and S. Bandyopadhyay, *Nano Lett.*, 2003, **3**, 397–401.
36 A. K. Galwey and M. E. Brown, *Thermochim. Acta*, 2002, **386**, 91–98.
37 H. Mirhosseini, C. P. Tan, N. S. Hamid and S. Yusof, *Food Hydrocolloids*, 2008, **22**, 1212–1223.
38 J. Zhu, L. Lu and K. Zeng, *ACS Nano*, 2013, **7**, 1666–1675.
39 X.-L. Yang, G. Peng, L.-L. Zhang, G. Liang, S. Duan, Y.-H. Huang, A. Ignatov and M. C. Croft, *J. Electrochem. Soc.*, 2012, **159**, A2096–A2099.
40 B.-K. Zou, H.-Y. Wang, Z.-Y. Qiang, Y. Shao, X. Sun, Z.-Y. Wen and C.-H. Chen, *Electrochim. Acta*, 2016, **196**, 377–385.

41 B. Wang, D. Wang, Q. Wang, T. Liu, C. Guo and X. Zhao, *J. Mater. Chem. A*, 2013, **1**, 135–144.
42 X. L. Wu, L. Y. Jiang, F. F. Cao, Y. G. Guo and L. J. Wan, *Adv. Mater.*, 2009, **21**, 2710–2714.
43 L. Hu, T. Zhang, J. Liang, Y. Zhu, K. Zhang and Y. Qian, *RSC Adv.*, 2016, **6**, 456–463.
44 H. Ni, J. Liu and L.-Z. Fan, *Nanoscale*, 2013, **5**, 2164–2168.
45 J. Song, B. Sun, H. Liu, Z. Ma, Z. Chen, G. Shao and G. Wang, *ACS Appl. Mater. Interfaces*, 2016, **8**, 15225–15231.